



## OPEN

## SUBJECT AREAS:

NANOWIRES

ELECTRONIC STRUCTURE

SURFACES, INTERFACES AND  
THIN FILMS

# Zn vacancy induced green luminescence on non-polar surfaces in ZnO nanostructures

F. Fabbri<sup>1</sup>, M. Villani<sup>1</sup>, A. Catellani<sup>1,2</sup>, A. Calzolari<sup>2</sup>, G. Cicero<sup>1,3</sup>, D. Calestani<sup>1</sup>, G. Calestani<sup>4</sup>, A. Zappettini<sup>1</sup>, B. Dierre<sup>5</sup>, T. Sekiguchi<sup>5</sup> & G. Salvati<sup>1</sup>Received  
3 April 2014Accepted  
9 May 2014Published  
4 June 2014Correspondence and  
requests for materials  
should be addressed to  
G.S. (giancarlo.  
salvati@cnr.it)

<sup>1</sup>IMEM-CNR Institute, Parco Area delle Scienze 37/A, 43124 Parma (Italy), <sup>2</sup>CNR-NANO, Istituto Nanoscienze, Centro S3, 41125 Modena, Italy, <sup>3</sup>Dipartimento Scienza Applicata e Tecnologia, Politecnico di Torino, Torino, Italy, <sup>4</sup>Dipartimento di Chimica GIAF, Università di Parma, Parco Area delle Scienze 17A, 43100 Parma (Italy), <sup>5</sup>Nano Device Characterization group, Advanced Electronic Materials Center, National Institute for Materials Science, 1-1 Namiki, Tsukuba, Ibaraki, 305-0044 (Japan).

Although generally ascribed to the presence of defects, an ultimate assignment of the different contributions to the emission spectrum in terms of surface states and deep levels in ZnO nanostructures is still lacking. In this work we unambiguously give first evidence that zinc vacancies at the (10 $\bar{1}0$ ) nonpolar surfaces are responsible for the green luminescence of ZnO nanostructures. The result is obtained by performing an exhaustive comparison between spatially resolved cathodoluminescence spectroscopy and imaging and *ab initio* simulations. Our findings are crucial to control undesired recombinations in nanostructured devices.

**Z**inc oxide (ZnO) one-dimensional nanostructures are of great interest for the development of devices in different fields, as energy harvesting<sup>1–4</sup>, chemical sensing<sup>5–7</sup>, optoelectronic devices like light emitting diodes<sup>8,9</sup>, solid state lasers<sup>10,11</sup> and plasmonic devices<sup>12,13</sup>.

Despite the high interest and expectation on ZnO-based devices, till nowadays they have been commercialized mainly for sensing applications. Other applications are still limited by a poor control of doping, in particular p-doping<sup>14</sup>, recombination, and contact stability<sup>15</sup>. For instance, in the case of optoelectronic devices, the comparison between ZnO and GaN, reveals the lower efficiency of ZnO-based devices with respect to those obtained with ZnO nanostructures on GaN substrates<sup>16</sup>. In photovoltaics, as well, energy conversion efficiencies reached with ZnO-based dye sensitized solar cells, are still much lower than those based on nanostructured TiO<sub>2</sub> films, notwithstanding the higher electronic mobility, and the broad availability of different ZnO nanostructure morphologies.

In nanostructured ZnO, the most controversial issue is the determination of chemical and/or crystallographic origin of the visible bands due to intra gap states in the emission spectra. Even though generally ascribed to the presence of defects, a precise assignment of these optical contributions is still lacking: both the experimental studies of defect emissions and theoretical simulations of the electronic structure and formation energy of different defects<sup>17–21</sup> have not yet provided a conclusive assessment. Briefly, the visible emissions can be divided in three colored bands: green, yellow and orange. The yellow and orange-red emissions are commonly attributed to the presence of excess oxygen in the samples<sup>22</sup> or to oxygen interstitial defects<sup>23–25</sup>, although some impurities such as Li may also play a role<sup>24</sup>.

The most common and controversial issue concerns the assignment of the green luminescence<sup>26,27</sup>. Different green luminescences are reported in the case of ZnO, depending on the peak position<sup>28</sup>. For instance it was demonstrated that the copper impurity in ZnO gives rise to a green luminescence peaked at 2.3 eV<sup>29</sup>. In addition the origin of the green luminescence, peaked at 2.5 eV, related to intrinsic point defects is still on debate<sup>28</sup>. The suppression of the 2.5 eV band upon surface coating or annealing<sup>30</sup> and the results from polarized luminescence measurements<sup>31</sup> seem to indicate that the defects involved are located at the surface<sup>32</sup>. However, there is no general consensus on the attribution of the chemical origin of these surface defects, alternatively assigned to Zn/O vacancies, impurities, surface reconstructions, etc (see e.g.<sup>30</sup> and references therein).

A controlled improvement of optoelectronic device performance can not leave out a microscopic understanding of ZnO surface states and deep levels. This is particularly true in low-dimensional nanostructures which have high surface-to-bulk ratio, and the effects of surface recombination are not limited to band-to-band recombi-



tion quenching, but may actually provide undesirable electron traps, detrimental for the photocurrent extraction<sup>32</sup>.

In order to gain insight on the microscopic origin of the green luminescence in ZnO, we propose a combined cathodoluminescence (CL) and *ab initio* study of ZnO one-dimensional nanostructures. To this aim, we compare nanorods (NR) and nanostructured thin films (NTF), to enhance different point defect contributions to the luminescence yield belonging to bare and buried surfaces. We furthermore compare experimental results and theoretical simulations in terms of defect formation energies and optical properties.

Our results unambiguously point out the determinant role of Zn vacancies ( $V_{Zn}$ ) on the green luminescence of ZnO nanostructures. In particular this study allows to link the origin of the green band to defects at the (10 $\bar{1}0$ ) surface of the nanostructures. This paves the way to control and reduce the undesired charge recombination in optical and electronic devices, such as photovoltaic systems, improving the photocurrent and the efficiency of the final device.

## Results

The high spatial resolution (about tens of nanometers) makes CL a unique tool for the simultaneous spectroscopic and emission mapping characterization of nanostructures<sup>33–36</sup>.

Fig. 1a shows a SEM image of a ZnO nanostructured thin film, consisting of grains with different sizes, whose average diameter is about 250 nm. Detailed grain-size statistics is reported in the SI (Figs. S1 and S2). From Fig. 1a two families of grains are identified, i.e. smaller and larger than 500 nm. All grains have a hexagonal section and terminate with a pyramid, which exposes six (10 $\bar{1}1$ ) surfaces. The CL emission spectra at room temperature are characterized by two typical features (Fig. 1d): the near-band edge (NBE) emission at 3.25 eV, due to band-to-band transitions including bound excitons

and shallow levels<sup>33</sup>, and the intra-gap states related green luminescence (GL) band centered at 2.5 eV.

The GL-to-NBE intensity ratio is commonly considered as a benchmark of the crystalline quality (point defects concentration), however this assumption can be misleading, as we will show below.

The spatial distribution of the NBE and GL emissions is investigated by CL imaging in Fig. 1b and 1c, respectively. All the grains have intense NBE emission that is quenched at grain boundaries. There is no dependence of the NBE emission on the size of the nano-grains: each grain shows a dark region at the tip of the hexagonal pyramid, suggesting that edge crossing favors the accumulation of non-radiative centers. The green luminescence is mainly localized at grain boundaries. The integrated intensity ratio between the NBE and GL emission is 0.768. Differently from NBE, the GL yield shows grain size dependence, i.e. the green luminescence is less intense in grains that exceed 500 nm, suggesting a dominant bulk-like behavior.

The observed XRD profile (Fig. 1e) depicts the diffraction pattern of the ZnO polycrystalline substrate, with strong orientation along the polar [0001] direction of the wurtzite structure and with minor contribution of other directions<sup>37</sup>: the diffraction peaks at about 31.7°, 34.4°, 36.1°, 62.8° are ascribable to the (10 $\bar{1}0$ ), (0002), (10 $\bar{1}1$ ) and (0004) planes, respectively, in good agreement with previous results<sup>38</sup>.

Changing the nanostructure morphology dramatically modifies the luminescence spatial distribution. Fig. 2a reports the SE micrograph of ZnO NR with 50 nm average diameters, NRs commonly exhibit hexagonal cross-section and expose well defined non-polar (10 $\bar{1}0$ ) surfaces. Further reducing the diameter leads to cylindrical-shaped nanostructures (see SI for further details).

Monochromatic maps of NBE and GL (panels b and c) demonstrate that the NBE emission is mainly due to the top surface of the hexagonal rod (most probably the polar (0001) surface); on the

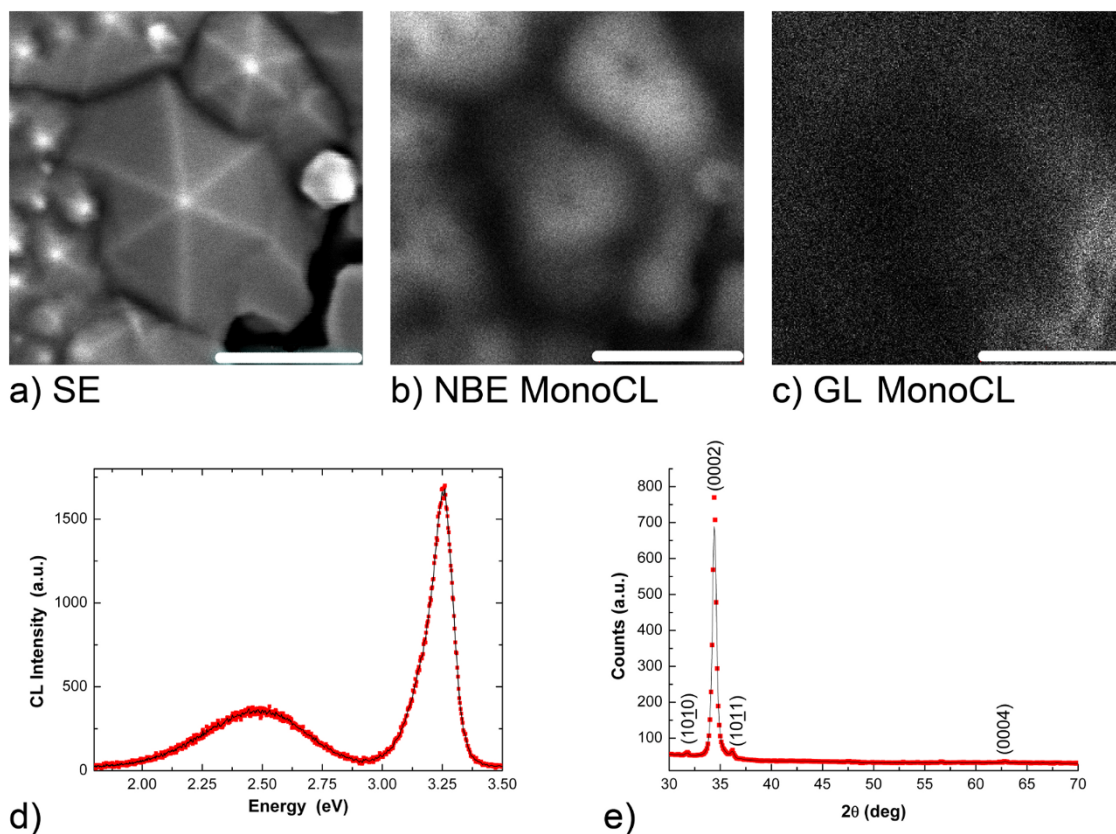


**Figure 1** | (a) Secondary electron micrograph of the ZnO thin film, (b) CL monochromatic map taken at ZnO NBE emission, (c) CL monochromatic map at ZnO GL emission; all the scalebars are 500 nm long. (d) CL spectrum and (e) XRD pattern.

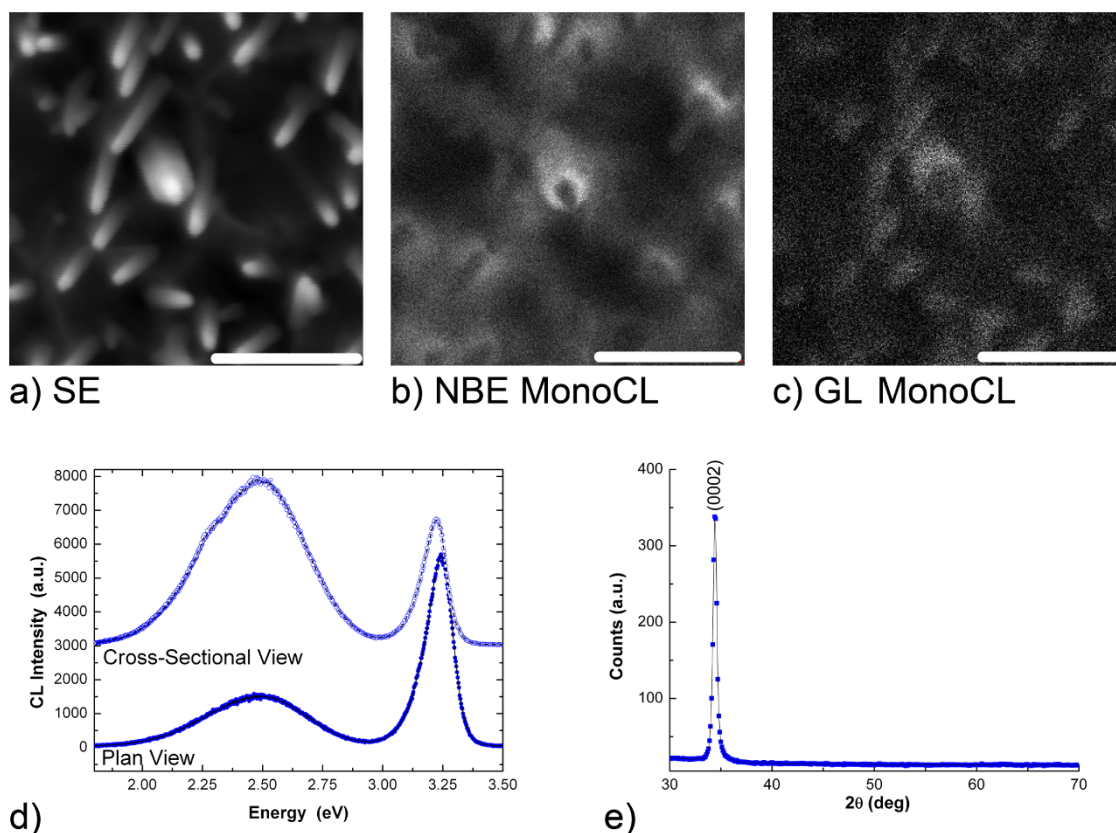


**Figure 2** | (a) Secondary electron micrographs of the ZnO nano-rods, (b) CL monochromatic map taken at ZnO NBE emission, (c) CL monochromatic map taken at ZnO GL emission; all the scalebars are 500 nm long. (d) CL spectrum obtained in the area under analysis in plan and cross-sectional view, (e) XRD pattern.

contrary, the GL signal comes lateral non-polar (10 $\bar{1}0$ ) surfaces of the hexagonal rods.

Fig. 2d shows the CL spectra of nanorods, obtained in planar and in cross-sectional modes: in the former analysis the GL-to-NBE ratio is 0.875, in latter it is increased to 4.53. The XRD pattern consists of a single peak corresponding to the (0002) reflection, which is a fingerprint of a high alignment of the nanorods on the substrate<sup>39</sup>.

Fig. 3a shows the SE images of the NR in cross-sectional view, panels 3b and 3c the NBE and GL maps, respectively. The CL intensity profiles are shown in Figure S3 of Supporting Information. The substrate displays an intense NBE emission and a faint GL luminescence.

Taking advantage of the high spatial resolution of CL technique, the evolution of the emission spectra along a single NR is analyzed. Fig. 3a indicates the spatial positions that correspond to the spot-mode CL spectra reported in Fig. 3d. CL results point out a decreasing of the NBE signal moving from the substrate to the tip of the wire. The intensity of the GL emission shows an opposite trend, it increases moving toward the NR tip (see SI Fig. S4 for additional results). For sake of clarity, the CL bands intensity trends are summarized in Fig. 3e.

To gain an in-depth understanding of the problem, we performed first principles simulations of the structural and electronic properties of prototypical defective ZnO systems, via systematic calculations based on density functional theory (DFT). In particular, we investigated Zn vacancies ( $V_{Zn}$ ), O vacancies ( $V_O$ ), H interstitials ( $H_{int}$ ), (and combinations of them), focusing on how the presence of point defects states affects the electronic properties of the compound. Our results are summarized in Fig. 4.

Here we compare different bulk calculations with the same defect concentration (0.8%) in terms of density of states (DOS) of the

defective systems. The neutral oxygen vacancies are associated to the formation of a donor-like occupied state, responsible for a shift at higher energy of the Fermi level,  $E_F$  (see red dotted line in topmost panel). This is, however, a deep defect, whose energy level is  $\sim 1$  eV below the conduction band bottom. Since the green luminescence corresponds to energy transitions of  $\sim 2.3$  eV, it is rather unlikely that this defect can be responsible for the observed green luminescence.

On the contrary, the presence of neutral Zn vacancies ( $V_{Zn}$ ) generates a multiple effect: the absence of Zn ions leaves out under-coordinated O atoms, and the unpaired O electrons give rise to empty states at  $E_F$ , close to the valence band top (black dashed line in both bulk -top panel- and surface -bottom panel) and to a residual spin magnetization<sup>40,41</sup>. As a consequence, this leads to a low density of empty states that may act as electron acceptor in the emission process. These results not only reveal that Zn vacancies are the most probable responsible of the green luminescence, in agreement with other theoretical results<sup>19</sup>; but also rule out the possibility that  $V_O$  can be associated with the green band. Our findings furthermore explain the reason of a possible misinterpretation of optical spectra in previous reports and their attribution to oxygen vacancies: Even though generated by a Zn vacancy, the defect-state appearing in the band gap has mainly an O-character, since it derives from unsaturated O dangling bonds (See Supplementary Information - Fig. S7).

Similar considerations apply to the electronic properties of the (10 $\bar{1}0$ ) surface (see Fig. 4, bottom panel). It was proved<sup>18,42</sup> that O vacancies at the non-polar (10 $\bar{1}0$ ) surface do not lead to significant features in the electronic properties, at least close to band edges. On the contrary, if a complex composed by a Zn + O vacancy was formed, a dispersionless filled defect band appears at the valence band top, reducing the band-gap. Here we further show that, in



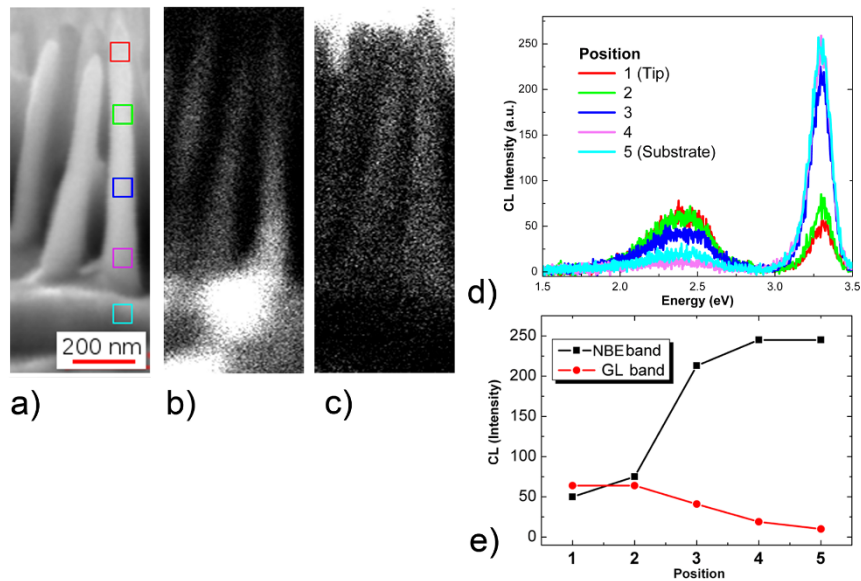


**Figure 3** | (a) Secondary electron micrographs of the ZnO nanorods in cross-sectional view with the indication of the positions in which has been carried a spot-mode CL spectrum, (b) CL monochromatic map taken at ZnO NBE emission, (c) CL monochromatic map taken at ZnO GL emission; all the scalebars are 200 nm long. (d) CL spectra of the different positions. Same color code is used. (e) Intensity trends as function of the position, on the top axis is shown the distance from the substrate.

the case of a single Zn surface vacancy, the inclusion of spin polarization induces a strong rehybridization of the O-derived orbitals and consequently a ferromagnetic behavior, in agreement with previous theoretical investigations<sup>41,43</sup>.

Finally, we calculated the formation energy of Zn vacancies at different positions in the slab, as summarized in Fig. 5. Our results reveal that Zn vacancies are much more probable close to the surface ( $\sim 1$  eV lower energy) for the formation of the defect at a (1010) surface with respect to inner positions in the slab. Furthermore,

the *n*-type character of the sample, as described by the presence of  $H_{int}$  in our simulations, is responsible for an increased stability (lower formation energy) of the point defect.

## Discussion

The comparison between NRs and NTF allows to achieve a better understanding of the ZnO light emission properties. (An additional intermediate family of nanostructure is reported in the Supplementary Information, Figure S5 and S6). First, the green luminescence is related to surface states generated by zinc vacancies, preferentially localized at non-polar (1010) surfaces. This assessment is supported by the comparison of the CL mapping of the single hexagonal NR with the NTF (Fig. 3 and Fig. 1 respectively) and by the increased stability (lower formation energy) of this kind of defects at surfaces (See Fig. 5). Indeed interface reconstruction at the grain boundaries can promote atomic rearrangements responsible for saturation of dangling bond states associated to  $V_{Zn}$  and finally for quenching of the GL.

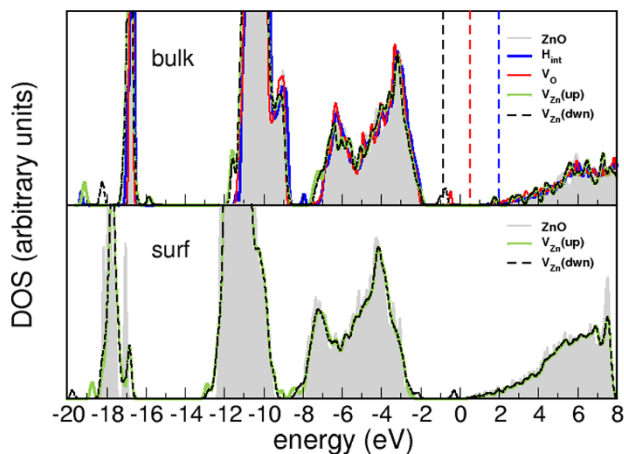


**Figure 4** | Electronic properties (density of states - DOS) of defective ZnO bulk (top) and (1010) surface (bottom panel), superimposed to the corresponding non-defective ZnO DOS in grey as obtained from first principles simulations. In the topmost panel different defects, at similar content ( $\sim 1\%$ ), are compared, namely  $V_{Zn}$  (green, up- and down-black dashed- spin contributions)  $V_O$  (red) and interstitial H ( $H_{int}$  in blue). The perfect clean bulk ZnO Fermi Level ( $E_F$ ) is taken as the zero of the energy scale; dotted lines in the different colors mark the Fermi Level for the different defected systems. Only  $H_{int}$  can be responsible for *n*-type doping, while neutral stoichiometry defects such as  $V_{Zn}$  and  $V_O$  give rise to deep level states. A similar behavior is obtained in surface calculations (bottom panel).

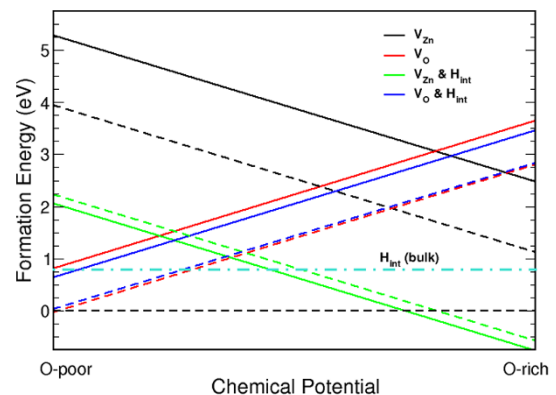


**Figure 5** | Formation energy of different defects in ZnO bulk (continuous line) and surface (dotted line), as obtained from first principles simulations<sup>44,45</sup>. Our results fairly compare with<sup>46,47</sup>. The effect of interstitial hydrogen (whose formation energy is indicated with a dotted cyan line) further increases stability of the defects (the formation energy decreases) and  $V_{Zn}$  appears to be to stable in Zn-poor (O-rich) conditions.



The analysis of the luminescence along the nanorod (Fig. 4) adds interesting details; a clear modification of the NBE-GL intensity ratio along the NR and in the planar/cross-sectional views is recorded i.e. NBE emission is lowered moving from the base to the tip of the NRs. Accordingly, the assessment of ZnO crystalline quality simply on the basis of the ratio between the NBE and GL may be misleading; indeed, this ratio is not inherently related to surface defects, since the intensity of the green band remarkably depends on the specific surface-to-volume ratio and morphology of the samples. This effect is in agreement with recent cathodoluminescence results on single crystal mesoporous ZnO nano-belts<sup>48</sup>.

Our joint analysis supports a comprehensive picture, which connects optical and morphological properties of the nanostructure. The intra-gap acceptor states originate by intrinsic Zn vacancies, preferentially formed on the lateral (1010) surface of the hexagonal NR. The absence of Zn ions modifies the charge state of the neighboring oxygen atoms, and imparts a local electron-deficiency at the surface, which easily reacts to restore the charge neutrality.

Our results on a variety of morphologies support the hypothesis that the presence of the green band is associated to Zn vacancies. In particular, our self-catalyzed growth technique is well compatible with a non-homogeneous defect distribution along the nanorod (in Fig. 3) and the consequent spatial variation of the luminescence intensity<sup>49,50</sup>. Indeed, it is highly probable that during self-catalyzed growth the nanorod becomes poor in zinc, favoring the formation of the zinc vacancies moving toward the NR tip. The increase in the intensity of the GL along the nanowires (Fig. 3) and the consequent decrease of the NBE emission are thus the consequences of a gradient of concentration of the Zn defects: this behavior is strictly related to the growth mechanism<sup>51</sup>.

## Conclusions

Our combined cathodoluminescence and ab initio study of ZnO one-dimensional nanostructures exposing different surfaces solves the existing controversy on the green luminescence origin in ZnO, assigning a determinant role to  $V_{Zn}$ . CL spectroscopy and imaging reveal that the ZnO green band is related to states at the (1010) non-polar surfaces, where  $V_{Zn}$  is found to be particularly stable. Emission in ZnO nanostructures with high aspect ratio are thus ultimately recast in terms of this defect.

## Methods

**Nanostructure synthesis.** ZnO-NR are grown by the optimized vapor phase technique described in Ref. 51 directly on the ZnO seed layer obtained by pulsed electron deposition<sup>38</sup>. Commercial Zn (powder, Sigma Aldrich, 4.5N) is used as source material after a smooth etching in diluted HCl. The source material and substrates are placed side-by-side in a tubular furnace, with the substrates in the downstream position and the source material inside a quasi-closed container (with only a small window for Zn vapor production). The growth temperature is limited to 480°C to be compatible with the glass substrates while Ar is used as an inert transporting gas. The furnace is kept at the working temperature for 1–5 minutes and then O<sub>2</sub> is introduced into the reactor for oxidation (1 : 20 O<sub>2</sub> to Ar ratio, 50 sccm) for 5 more minutes. Finally, the furnace is cooled down and samples collected. As previously reported<sup>51</sup>, the morphology of different ZnO nanostructures depends drastically on the first growing step during which zinc droplets are formed onto the substrate<sup>51</sup>; to vary droplet size and distribution, we controlled and changed systematically the delay before O<sub>2</sub> introduction.

**Characterization.** The CL spectroscopy and imaging are carried out with Horiba CL system equipped on a Hitachi 4200 FEG-SEM. The accelerating voltage is 5 keV and the beam current is 400 pA. All the experiments are carried out at room temperature. Additional details are reported in the Supporting Information. All integrated intensities are summarized in Table S1 of Supporting Information.

XRD patterns are recorded using a Thermo Scientific (Thermo ARL X'tra) with Bragg-Brentano  $\theta$ - $\theta$  configuration with a maximum 2 $\theta$  excursion ranging from  $-8^\circ$  and  $180^\circ$ . X-Ray source is Cu K $\alpha$  ( $\lambda = 1.542 \text{ \AA}$ ) and the accelerating voltage is set in the range 20 ÷ 40 kV. Diffracted rays are collected through a solid state Si:Li detector cooled by Peltier element.

**Calculations.** First principles simulations of the structural and electronic properties of prototypical ZnO bulk and surface defective structures were performed to complement the experiments: our calculations are based on Density Functional

Theory (DFT), in the plane wave and pseudopotential description, as implemented in the QUANTUM-ESPRESSO suite<sup>52</sup>. Since the application of DFT to ZnO is known to produce a severe underestimation of the electronic band gap due to unphysical interaction between the Zn *d*-orbitals and the O *sp*-bands, we employ the DFT + U scheme to properly compute the electronic structure. See Supporting Information (SI) for technical details.

- Zhang, Q., Dandeneau, C. S., Zhou, X. & Cao, G. ZnO Nanostructures for Dye-Sensitized Solar Cells. *Adv. Mater.* **21**, 4087–4108 (2009).
- Wang, Z. L. & Song, J. Piezoelectric Nanogenerators Based on Zinc Oxide Nanowire Arrays. *Science* **312**, 242–246 (2006).
- Park, H. *et al.* Graphene Cathode-Based ZnO Nanowire Hybrid Solar Cells. *Nano Lett.* **13**, 233–239 (2012).
- Jean, J. *et al.* ZnO Nanowire Arrays for Enhanced Photocurrent in PbS Quantum Dot Solar Cells. *Adv. Mater.* **25**, 2790–2796 (2013).
- Wang, J. X. *et al.* Hydrothermally grown oriented ZnO nanorod arrays for gas sensing applications. *Nanotechnology* **17**, 4995–4998 (2006).
- Calestani, D. *et al.* Growth of ZnO tetrapods for nanostructure-based gas sensors. *Sens. Actuat. B-Chem* **144**, 472–478 (2010).
- WangWang, Summers, C. J. & Wang, Z. L. Large-Scale Hexagonal-Patterned Growth of Aligned ZnO Nanorods for Nano-optoelectronics and Nanosensor Arrays. *Nano Lett.* **4**, 423–426 (2004).
- Jeong, M.-C., Oh, B.-Y., Ham, M.-H. & Myoung, J.-M. Electroluminescence from ZnO nanowires in n-ZnO film/ZnO nanowire array/p-GaN film heterojunction light-emitting diodes. *Appl. Phys. Lett.* **88**, 202105 (2006).
- Könenkamp, R., Word, R. C. & Schlegel, C. Vertical nanowire light-emitting diode. *Appl. Phys. Lett.* **85**, 6004–6006 (2004).
- Huang, M. H. *et al.* Room-Temperature Ultraviolet Nanowire Nanolasers. *Science* **292**, 1897–1899 (2001).
- Yang, P. *et al.* Controlled Growth of ZnO Nanowires and Their Optical Properties. *Adv. Funct. Mater.* **12**, 323–331 (2002).
- Kim, H., Osofsky, M., Prokes, S. M., Glembocki, O. J. & Piqué, A. Optimization of Al-doped ZnO films for low loss plasmonic materials at telecommunication wavelengths. *Appl. Phys. Lett.* **102**, 171103 (2013).
- Naik, G. V., Shalae, V. M. & Boltasseva, A. Alternative Plasmonic Materials: Beyond Gold and Silver. *Adv. Mater.* **25**, 3264–3294 (2013).
- Look, D. C. & Clafin, B. P-type doping and devices based on ZnO. *Phys. Status Solidi b* **241**, 624–630 (2004).
- Catellani, A., Calzolari, A. & Ruini, A. Effect of ultrathin gold on the Ohmic-to-Schottky transition in Al/ZnO contacts: A first-principles investigation. *J. Appl. Phys.* **115**, 043711 (2014).
- Ozgur, U., Hofstetter, D. & Morkoc, H. ZnO Devices and Applications: A Review of Current Status and Future Prospects. *P. IEEE* **98**, 1255–1268 (2010).
- Calzolari, A., Bazzani, M. & Catellani, A. Dipolar and charge transfer effects on the atomic stabilization of ZnO polar surfaces. *Surf. Sci.* **607**, 181–186 (2013).
- Calzolari, A. & Catellani, A. Water Adsorption on Nonpolar ZnO(1010) Surface: A Microscopic Understanding. *J. Phys. Chem. C* **113**, 2896–2902 (2009).
- Janotti, A. & Van de Walle, C. G. Native point defects in ZnO. *Phys. Rev. B* **76**, 165202 (2007).
- Catellani, A., Ruini, A., Cicero, G. & Calzolari, A. First principles description of the electronic properties of doped ZnO. *Phys. Status Solidi A* **250**, 2106–2109 (2013).
- Janotti, A. & Van de Walle, C. G. Oxygen vacancies in ZnO. *Appl. Phys. Lett.* **87**, 122102 (2005).
- Cross, R. B. M., Souza, M. M. D. & Narayanan, E. M. S. A low temperature combination method for the production of ZnO nanowires. *Nanotechnology* **16**, 2188–2192 (2005).
- Greene, L. E. *et al.* Low-Temperature Wafer-Scale Production of ZnO Nanowire Arrays. *Angew. Chem. Int. Ed.* **42**, 3031–3034 (2003).
- Li, D. *et al.* Different origins of visible luminescence in ZnO nanostructures fabricated by the chemical and evaporation methods. *Appl. Phys. Lett.* **85**, 1601–1603 (2004).
- Liu, X., Wu, X., Cao, H. & Chang, R. P. H. Growth mechanism and properties of ZnO nanorods synthesized by plasma-enhanced chemical vapor deposition. *J. Appl. Phys.* **95**, 3141–3147 (2004).
- Reynolds, D. C., Look, D. C., Jogai, B. & Morkoc, H. Similarities in the bandedge and deep-centre photoluminescence mechanisms of ZnO and GaN. *Solid State Commun.* **101**, 643–646 (1997).
- Djurišić, A. B. *et al.* Defect emissions in ZnO nanostructures. *Nanotechnology* **18**, 095702 (2007).
- Özgür, Ü. *et al.* A comprehensive review of ZnO materials and devices. *J. Appl. Phys.* **98**, 041301 (2005).
- Alivov, Y. I., Chukichev, M. V. & Nikitenko, V. A. Green luminescence band of zinc oxide films copper-doped by thermal diffusion. *Semiconductors* **38**, 31–35 (2004).
- Djurišić, A. B. & Leung, Y. H. Optical Properties of ZnO Nanostructures. *Small* **2**, 944–961 (2006).
- Hsu, N. E., Hung, W. K. & Chen, Y. F. Origin of defect emission identified by polarized luminescence from aligned ZnO nanorods. *J. Appl. Phys.* **96**, 4671–4673 (2004).
- Shalish, I., Temkin, H. & Narayanamurti, V. Size-dependent surface luminescence in ZnO nanowires. *Phys. Rev. B* **69**, 245401 (2004).



33. Lazzarini, L. *et al.* Unpredicted Nucleation of Extended Zinc Blende Phases in Wurtzite ZnO Nanotetrapod Arms. *ACS Nano* **3**, 3158–3164 (2009).
34. Yan, J. *et al.* Structure and Cathodoluminescence of Individual ZnS/ZnO Biaxial Nanobelt Heterostructures. *Nano Lett.* **8**, 2794–2799 (2008).
35. Lee, W. W., Kim, S. B., Yi, J., Nichols, W. T. & Park, W. I. Surface Polarity-Dependent Cathodoluminescence in Hydrothermally Grown ZnO Hexagonal Rods. *J. Phys. Chem. C* **116**, 456–460 (2011).
36. Foley, M., Ton-That, C. & Phillips, M. R. Cathodoluminescence inhomogeneity in ZnO nanorods. *Appl. Phys. Lett.* **93**, 243104 (2008).
37. Foley, M., Ton-That, C. & Phillips, M. R. Luminescent properties of ZnO structures grown with a vapour transport method. *Thin Solid Films* **518**, 4231–4233 (2010).
38. Calestani, D. *et al.* Solution-free and catalyst-free synthesis of ZnO-based nanostructured TCOs by PED and vapor phase growth techniques. *Nanotechnology* **23**, 194008 (2012).
39. Sun, Y., Fuge, G. M. & Ashfold, M. N. R. Growth of aligned ZnO nanorod arrays by catalyst-free pulsed laser deposition methods. *Chem. Phys. Lett.* **396**, 21–26 (2004).
40. Chaboy, J. *et al.* Evidence of intrinsic magnetism in capped ZnO nanoparticles. *Phys. Rev. B* **82**, 064411 (2010).
41. Wang, Q., Sun, Q., Chen, G., Kawazoe, Y. & Jena, P. Vacancy-induced magnetism in ZnO thin films and nanowires. *Phys. Rev. B* **77**, 205411 (2008).
42. Calzolari, A., Ruini, A. & Catellani, A. Anchor Group versus Conjugation: Toward the Gap-State Engineering of Functionalized ZnO(1010) Surface for Optoelectronic Applications. *J. Am. Chem. Soc.* **133**, 5893–5899 (2011).
43. Hong, N. H., Sakai, J. & Brizé, V. Observation of ferromagnetism at room temperature in ZnO thin films. *J. Phys.-Condens. Matt.* **19**, 036219 (2007).
44. Qian, G.-X., Martin, R. M. & Chadi, D. J. First-principles study of the atomic reconstructions and energies of Ga- and As-stabilized GaAs(100) surfaces. *Phys. Rev. B* **38**, 7649–7663 (1988).
45. Van de Walle, C. G. & Neugebauer, J. First-principles calculations for defects and impurities: Applications to III-nitrides. *J. Appl. Phys.* **95**, 3851–3879 (2004).
46. D'Amico, N. R., Cantele, G. & Ninno, D. First-Principles Calculations of Clean and Defected ZnO Surfaces. *J. Phys. Chem. C* **116**, 21391–21400 (2012).
47. Erhart, P., Albe, K. & Klein, A. First-principles study of intrinsic point defects in ZnO: Role of band structure, volume relaxation, and finite-size effects. *Phys. Rev. B* **73**, 205203 (2006).
48. Nasi, L. *et al.* Mesoporous single-crystal ZnO nanobelts: supported preparation and patterning. *Nanoscale* **5**, 1060–1066 (2013).
49. Nobis, T. *et al.* Spatially Inhomogeneous Impurity Distribution in ZnO Micropillars. *Nano Lett.* **4**, 797–800 (2004).
50. Yuan, X. L., Dierre, B., Wang, J. B., Zhang, B. P. & Sekiguchi, T. Spatial Distribution of Impurities in ZnO Nanotubes Characterized by Cathodoluminescence. *J. Nanosci. Nanotechnol.* **7**, 3323–3327 (2007).
51. Calestani, D., Zha, M. Z., Zanotti, L., Villani, M. & Zappettini, A. Low temperature thermal evaporation growth of aligned ZnO nanorods on ZnO film: a growth mechanism promoted by Zn nanoclusters on polar surfaces. *CrystEngComm* **13**, 1707–1712 (2011).
52. Giannozzi, P. *et al.* QUANTUM ESPRESSO: a modular and open-source software project for quantum simulations of materials. *J. Phys.-Condens. Matt.* **21**, 395502 (2009).

## Acknowledgments

Dr. Fabbri wants to thank Mr. P. Rekemeyer of the Department of Material Science and Engineering at the Massachusetts Institute of Technology, for the useful discussions about zinc oxide nanostructures and the possible development of ZnO based solar cells. The research leading to these results has received funding from the European Union Seventh Framework Programme under grant agreement n° 265073 (ITN-Nanowiring). Computer time was provided by CINECA through ISCRA projects.

## Author contributions

The manuscript was written through contributions of all authors. All authors gave approval to the final version of the manuscript. FF and BD carried out the CL experiments under the supervision of GS and TS. MV, DC carried out the growth of the nanostructures under the supervision of AZ. G. Cal carried out the XRD analysis. AC, AC and GC performed the theoretical calculations.

## Additional information

**Supplementary information** accompanies this paper at <http://www.nature.com/scientificreports>

**Competing financial interests:** The authors declare no competing financial interests.

**How to cite this article:** Fabbri, F. *et al.* Zn vacancy induced green luminescence on non-polar surfaces in ZnO nanostructures. *Sci. Rep.* **4**, 5158; DOI:10.1038/srep05158 (2014).



This work is licensed under a Creative Commons Attribution-NonCommercial-NoDerivs 4.0 International License. The images or other third party material in this article are included in the article's Creative Commons license, unless indicated otherwise in the credit line; if the material is not included under the Creative Commons license, users will need to obtain permission from the license holder in order to reproduce the material. To view a copy of this license, visit <http://creativecommons.org/licenses/by-nc-nd/4.0/>